machines

MDPI

Article

Stator Structures and Models of Using Grain-Oriented Electrical Steels for High-Power-Density PMSMs

Guanglin Li [1,2], Jing Zhao [1,*], Xiaoqing Guan [3], Jianguo Zhu [4] and Zhiyuan Hu [2]

[1] School of Automation, Beijing Institute of Technology, Beijing 100081, China
[2] Shougang Zhixin Electromagnetic Material (Qian'an) Co., Ltd., Tangshan 064400, China
[3] Department of Intelligent Control, Yantai Engineering & Technology College, Yantai 264006, China
[4] School of Electrical and Information Engineering, University of Sydney, Sydney, NSW 2006, Australia; jianguo.zhu@sydney.edu.au
* Correspondence: zhaojing_bit@bit.edu.cn

Abstract

This article studies different stator structures and modeling methods for using grain-oriented electrical steels (GOES) to improve the performance of high-power-density permanent magnet synchronous motors (PMSMs). The magnetic characteristics of GOES samples are measured under magnetizations at different angles and frequencies. Models of various GOES stator teeth and yokes are established. The effects of different GOES stators on PMSM performance are studied, and their advantages and disadvantages are compared. Three typical GOES PMSM prototypes are fabricated and tested to demonstrate the superiority of GOES stators and validate the effectiveness of the established models.

Keywords: PMSM; grain-oriented electrical steels; magnetic property; stator topology; models of GOES

1. Introduction

To develop high-performance electrical drive systems for advanced applications, such as electric vehicles, all-electric aircraft, and robotic systems, while complying with increasingly stringent environmental standards, the focus on electrical motors is increasingly shifting toward achieving high power density (i.e., small size and lightweight for a given capacity) and high efficiency [1–3]. Among various types of electrical motors, permanent magnet synchronous motors (PMSMs) provide superior power density and efficiency, making them increasingly popular for high-performance applications [4–6]. However, their performance is limited by stator cores made of non-grain-oriented electrical steel (NOES) sheets (or non-oriented electrical steel sheets for short), which are isotropic but have low permeability and high core losses, especially when operated at high speeds.

Amorphous alloys exhibit high permeability and low core losses at high frequencies and, thus, are suitable for high-speed PMSMs [7,8]. However, their application is hindered by the difficulty in the mechanical manufacturing of amorphous alloy stator cores. Attempts have been made to develop high-speed PMSMs with 3D magnetic fluxes using soft magnetic composites [9,10], but their low magnetic permeability constrains further performance improvement.

High-strength electrical sheet steel is employed to strengthen the motor structure at high speeds [11]. Although the electromagnetic characteristics are poorer than those of NOES sheets, using such material enables the design of diverse topologies for high-speed operations.

Check for updates

Academic Editors: Yiming Shen, Xuhui Zhu and Shengdao Zhu

Received: 19 December 2025
Revised: 20 January 2026
Accepted: 22 January 2026
Published: 27 January 2026

Copyright: © 2026 by the authors. Licensee MDPI, Basel, Switzerland. This article is an open access article distributed under the terms and conditions of the Creative Commons Attribution (CC BY) license.

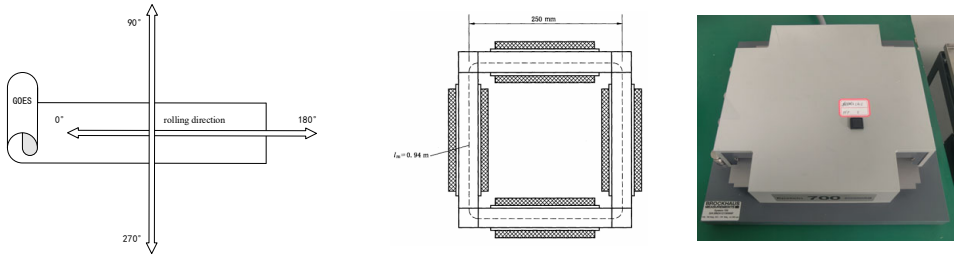
In contrast to NOES sheets, grain-oriented electrical steel (GOES) sheets are anisotropic, with very high permeability and low core losses in the rolling direction. Some hybrid motor structures using both NOES and GOES sheets have been developed to take advantage of these superior characteristics along the rolling direction. A novel PM-assisted synchronous reluctance motor was developed by constructing selected stator teeth with GOES sheets to mitigate issues related to stator tooth saturation [12]. This method yields improved efficiency, a broader operational speed range, and a 7% increase in torque capacity. References [13,14] delved into the application of GOES in synchronous reluctance motors. GOES has been used in an in-wheel split-teeth dual PM vernier motor to significantly reduce core losses while enhancing efficiency and torque density [15]. A dual-rotor axial-flux PM motor with GOES stator teeth is designed for electric aircraft [16]. Various studies of PMSMs with hybrid GOES and NOES stators show that the motors employing GOES in the stator exhibit superior torque density and efficiency [17,18]. The multi-physics performance characteristics of GOES motors have been assessed for potential applications in new energy vehicles [19]. GOES has been used in different rotor and stator magnetic circuit segments to reduce material waste and enhance manufacturing automation through modular structures [20].

In summary, current research predominantly focuses on the feasibility and prospects of applying GOES in motors. The computational magnetic field and electromagnetic performance analysis models still follow those of traditional NOES motors. More complex models must be developed systematically to account for the strong anisotropic magnetic properties and complicated stator topological structures of GOES PMSMs.

This paper explores various topological structures and modeling methods for PMSM stators with GOES based on a comprehensive study and understanding of GOES magnetic characteristics. Three typical GOES PMSM prototypes are designed and manufactured. The prototypes are tested to demonstrate the superior performance of GOES stators and validate the authenticity and accuracy of the proposed models.

2. Directional Characteristics of GOES

GOES, also known as cold-rolled GOES, refers to electrical steel with a specific crystalline structure exhibiting strong anisotropic magnetic properties with the highest permeability and lowest core loss in the rolling direction, as shown in Figure 1a. A comprehensive study is conducted to understand GOES magnetic characteristics in different magnetization directions using an Epstein Frame, as shown in Figure 1b,c. When measuring the magnetic characteristics of GOES at different angles, the GOES can be placed at different inclined angles for measurement. The results are shown in Figures 2–4.



(**a**) (**b**) (**c**)

Figure 1. Schematic diagram of GOES rolling process and magnetic characteristic test method: (**a**) schematic diagram of the rolling direction of GOES; (**b**) Epstein Frame; and (**c**) test equipment.

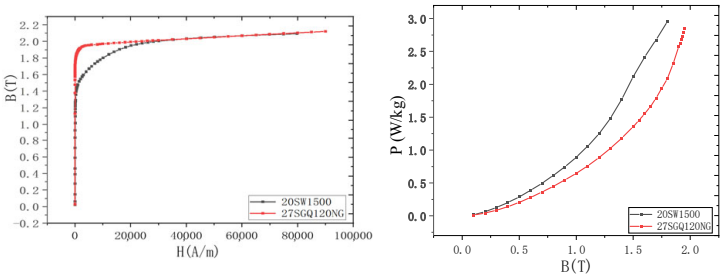


Figure 2. Comparison of magnetic characteristics between GOES (27SGQ120NG) and NOES (20SW1500) in the rolling direction: (**a**) B-H curve; (**b**) P-B curve.

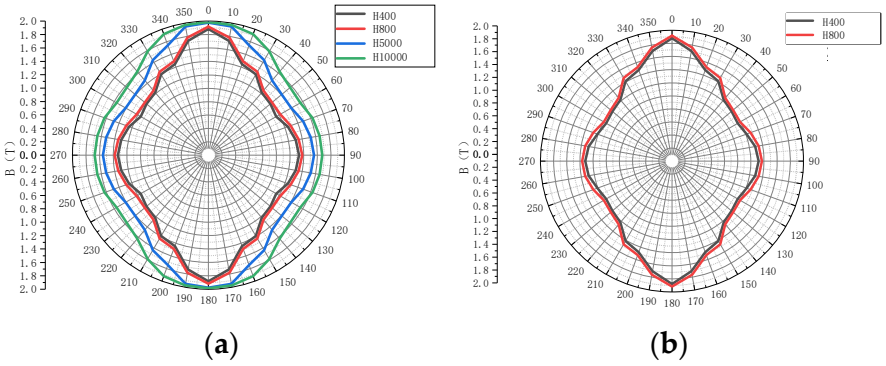


Figure 3. B versus H of GOES 27SQG120 in different directions: (**a**) 50 Hz; (**b**) 1000 Hz.

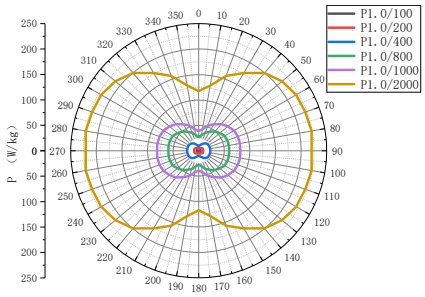


Figure 4. Specific core loss vs. frequency curves of GOES 27SQG120 at 1.0 T in different directions.

Figure 2 compares the magnetic characteristics of typical GOES (27SGQ120NG) and NOES (20SW1500) in the rolling direction. Under the same testing conditions, GOES exhibits higher magnetic permeability, which is defined as the ratio of magnetic flux density B (T) and magnetic field strength H (A/m), and lower specific core loss, P (W/kg), than NOES.

Figure 3 shows B versus H of GOES 27SQG120 in different directions when H = 400 A/m, 800 A/m, 5000 A/m, and 10,000 A/m at 50 Hz and 1000 Hz. As shown, the shapes of the B versus H curves at different frequencies are similar, resembling a spindle shape with the maximum at 0° and 180° and the minimum at 60°, 120°, 240°, and 300° from the rolling direction. Figure 3a shows that as H increases, the difference in B in different directions becomes smaller, and the B curve approaches a more circular shape as the sample saturates.

Figure 4 plots the specific core loss versus frequency curves of GOES 27SQG120 at 1.0 T in different directions. In a given direction, the core loss increases dramatically for a given B as the frequency increases. However, at any frequency, the core loss is always the smallest in the rolling directions of 0° and 180°, and the maximal core loss always

occurs at angles approximately perpendicular to the rolling direction, such as 80°, 100°, 260°, and 280°.

3. Topological Structure Design of the GOES Stator

Because of the strong anisotropy of GOES, in a stator core containing both NOES and GOES, the angle between the magnetic flux lines and the rolling direction of the GOES determines the magnetization characteristics and loss properties of the stator core, which in turn affects the motor performance.

The physical motor topologies designed in this paper are limited to three types: snap-on stator teeth (SOST) motor, dovetail-slot stator teeth (DSST) motor, and teeth–yoke integrated stator (TYIS) motor. SOST corresponds to Figure 5a, DSST corresponds to Figure 5b–j, and TYIS corresponds to Figure 5k–o. There are different manufacturing methods for the same type of motor, full-circle stator yoke (FCSY) and fan-shape stator yoke (FSSY).

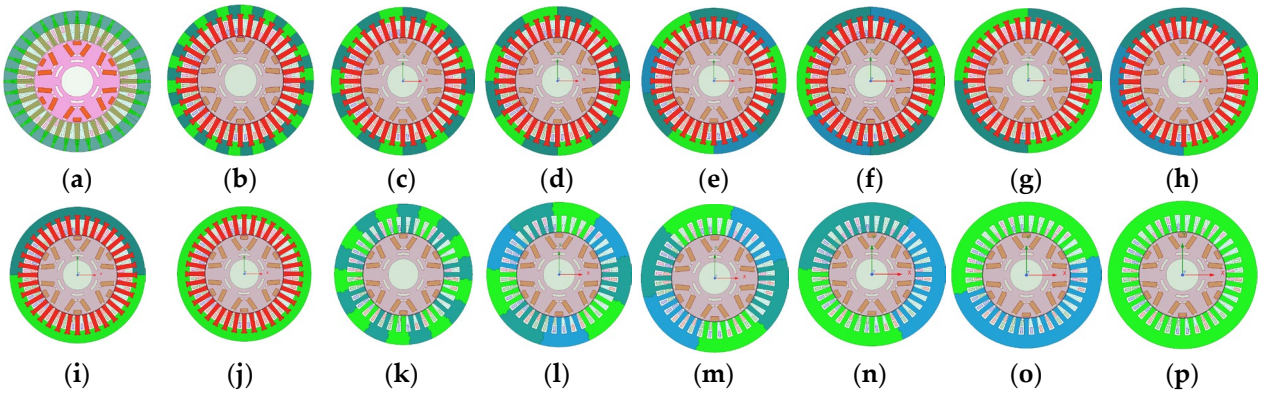
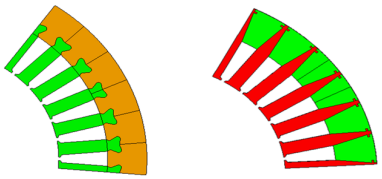


Figure 5. GOES stator topological structures: (**a**) SOST motor; (**b**) DSST motor, yoke in 36 parts; (**c**) DSST motor, yoke in 18 parts; (**d**) DSST motor, yoke in 12 parts; (**e**) DSST motor, yoke in 9 parts; (**f**) DSST motor, yoke in 6 parts; (**g**) DSST motor, yoke in 4 parts; (**h**) DSST motor, yoke in 3 parts; (**i**) DSST motor, yoke in 2 parts; (**j**) DSST motor, yoke in 1 part; (**k**) TYIS motor, stator in 18 parts; (**l**) TYIS motor, stator in 9 parts; (**m**) TYIS motor, stator in 6 parts; (**n**) TYIS motor, stator in 3 parts; (**o**) TYIS motor, stator in 2 parts; and (**p**) motor with integrated NOES stator.

Figure 5a,b are adopted in Section 4 to investigate the modeling method for the stator teeth of grain-oriented silicon steel motors. Figure 5b–j are employed in Section 5 to explore the modeling method for the stator yokes of grain-oriented silicon steel motors. Figure 5k–p are utilized in Section 6, where the modeling methods developed in Chapters 4 and 5 are applied to analyze the performance differences of grain-oriented silicon steel motors with different topologies, and a comparative study is conducted with traditional non-oriented silicon steel motors.

4. Modeling Method for GOES Stator Teeth

Figure 6 shows two typical structures, DSST and SOST, for GOES stator teeth, where the yokes are made of NOES. GOES magnetization curves in different directions are employed to model the stator teeth of different angles. By analyzing and comparing the motor performance using different modeling methods, suitable models for GOES stator teeth are developed. When modeling, the same mesh refinement rules are set for all models, especially for the segmented regions of the stator teeth.

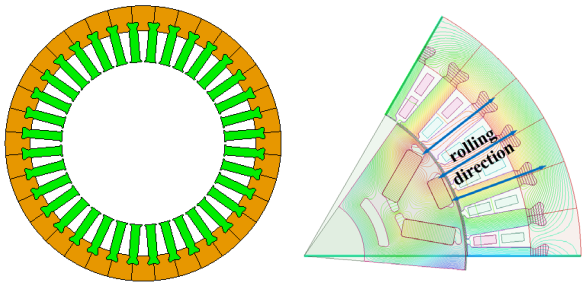


(**a**) (**b**)

Figure 6. Two typical GOES stator structures: (**a**) DSST; (**b**) SOST.

4.1. DSST

Figure 7 shows the stator structure and simulation model of a DSST motor. As shown in Figure 7a, the stator core is comprised of a yoke with 36 fan-shaped NOES (27SW1400) parts and 36 GOES (27SQG120) stator teeth embedded in dovetail slots between fan-shaped yoke parts.



(**a**) (**b**)

Figure 7. DSST stator and simulation model: (**a**) DSST stator core; (**b**) simulation model.

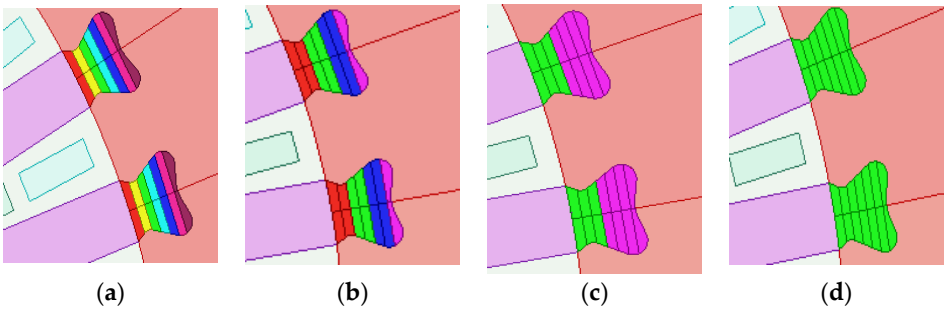
As is well known, the magnetic field lines of the motor are radial when passing through the stator teeth. To better utilize the characteristic of GOES with high magnetic permeability along the rolling direction, the rolling direction of the grain-oriented electrical steel in each tooth is aligned parallel to the radial direction. On the other hand, the shear direction of GOES is oriented tangentially to the motor stator, which does not constitute the main magnetic circuit for magnetic flux lines and thus has little impact on motor performance. The different angle-based segmentations mentioned in the following text refer to different modeling methods for the same motor structure. The motor simulation model in Figure 7b shows that the magnetic flux lines in the middle of the stator teeth are primarily radial, coinciding with the rolling direction of the GOES. Thus, when defining the material properties of this part of the model, the magnetization properties can be set according to the magnetization characteristics measured along the GOES rolling direction, as shown in Figure 3 at 0° or 180°.

In the DSST areas near the rotor surface, the magnetic flux lines are mostly radial and spread slightly to cover more rotor surface area. The material's magnetization properties should be defined based on data measured close to the rolling direction, such as those at 10° or 170° in Figure 3.

In the joint area of the yoke and stator teeth, the magnetic flux lines tend to be tangential, and the material's magnetization properties should be defined based on data measured perpendicular to the rolling direction, such as those at 90° or 270° in Figure 3.

For a given stator structure, the joint area of the stator teeth and yoke can be divided into 7, 4, 2, and 1 segments, as shown in Figure 8. To ensure consistent mesh division and structural variables, the same geometric model is used for different simulation methods. Different segmentations are distinguished by different colors, and areas with the same color

have the same magnetization properties. For the DSST stator, there are six methods for defining the magnetization properties, as follows:



(**a**) (**b**) (**c**) (**d**)

Figure 8. Segmentation of the DSST stator: (**a**) 7 segments; (**b**) 4 segments; (**c**) 2 segments; and (**d**) 1 segment.

Method 1: When the joint area is divided into 7 segments, as shown in Figure 8a, each segment is assigned different magnetization properties based on the angle between the magnetic flux lines and the rolling direction of GOES, as shown in Figure 9. In the red area, the magnetic flux lines are close to the rolling direction of GOES, with an angle of approximately 10°. Therefore, the material properties of the red area are defined according to the magnetization properties measured at 10° in Figure 3. Other areas are defined similarly. From the radial direction inward, the angles are 10°, 20°, 30°, 40°, 50°, 60°, and 70°.

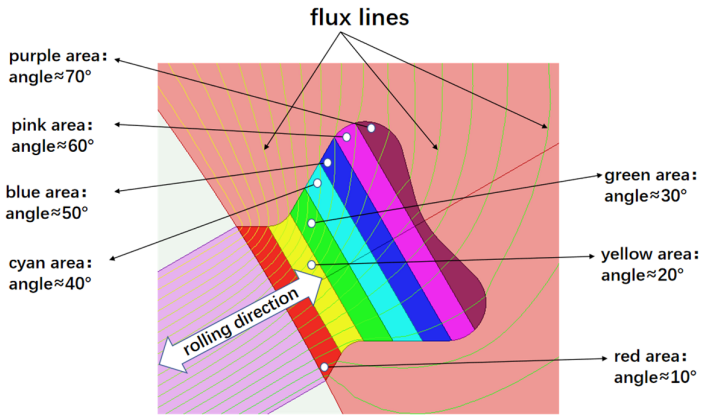


Figure 9. Magnetization properties for segmented and joint areas of the stator yoke and teeth when divided into 7 segments.

Method 2: When the joint area is divided into 4 segments, each segment is assigned magnetic properties based on the data measured at 10°, 30°, 50°, and 60° in Figure 3.

Method 3: When the joint area is divided into 2 segments, each segment is assigned magnetization properties based on the data measured at 30° and 60° in Figure 3.

Methods 4–6: When the joint area is considered 1 segment, the entire joint area's magnetization properties are assigned based on the data measured at 30°, 60°, and 90°, corresponding to methods 4–6, respectively.

The simulation results of modeling method 6 for the DSST deviate significantly from those of other modeling methods. The largest deviation is when the entire area is assigned the same value. When subdividing the area according to the direction of the magnetic circuit, the finer the subdivision, the more accurate the calculation results. For the sake of calculation convenience, regions with magnetic flux line direction that deviates from the radial direction by less than 60° can be defined as a single block and assigned the same

magnetic property. The simulation results will have a small deviation compared to the finely subdivided results. Regions where the magnetic flux line direction deviates from the radial direction by more than 60° have a more significant impact on the results and should be assigned values separately.

For accurate and convenient calculations, when designing motors, ensuring that the depth of the DSST does not exceed the bending point of the magnetic flux line direction can keep the angle between the magnetic flux line direction and the tooth rolling direction within 60°. This allows the joint area to be assigned the same magnetization properties in one block, simplifying the calculations.

Each method calculates motor performance under no-load, rated load, and overload. The electromagnetic performance, including the back electromotive force (EMF), E, air gap flux density, B_δ, cogging torque, T_{cog}, electromagnetic torque, T, and core loss, P_{Fe}, for the six modeling methods are summarized and compared in Table 1.

Table 1. Comparison of six DSST model methods.

States	Parameters	Method 1	Method 2	Method 3	Method 4	Method 5	Method 6
No-load	E (V)	254	252	254	253	253	246
	B_δ (T)	0.75	0.75	0.75	0.75	0.75	0.75
	T_{cog} (Nm)	0.400	0.540	0.401	0.488	0.495	0.471
Rated load	E (V)	364	351	363	377	375	366
	B_δ (T)	1.03	1.00	1.07	1.07	1.06	1.07
	T (Nm)	58.7	57	59	60	60	57
	P_{Fe} (W)	494	500	477	440	490	550
Overload	E (V)	354	347	353	358	356	346
	B_δ (T)	1.25	1.26	1.27	1.27	1.26	1.27
	T (Nm)	212	209	212	215	214	204
	P_{Fe} (W)	544	490	485	456	500	569

4.2. SOST

Figure 10 shows the stator core structure and simulation model of a SOST motor. The GOES stator teeth are embedded with a snap-on structure between two fan-shaped segments, as shown in Figure 10a. For the sections of the stator teeth not joining the yoke, the magnetization characteristics are defined as those measured in the rolling direction, as shown in Figure 10b. For the areas where the stator teeth join the yoke, the magnetization characteristics are defined according to the direction of the magnetic flux lines.

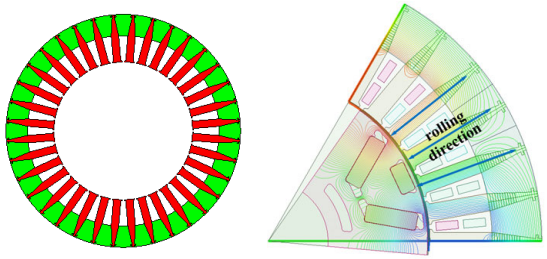
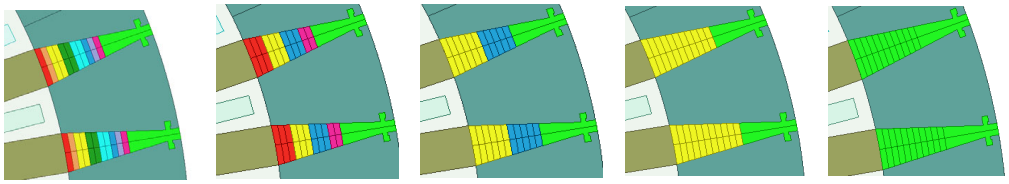


Figure 10. Stator core structure and simulation model of a SOST motor: (**a**) DSST stator core; (**b**) simulation model.

Figure 11 illustrates 5 cases of dividing the stator teeth–yoke joint area into different segments, where different colors mean different magnetization characteristics. There are six methods for defining the magnetization properties of cases, as follows:



(**a**) (**b**) (**c**) (**d**) (**e**)

Figure 11. Segmentation of the SOST stator: (**a**) 9 segments; (**b**) 5 segments; (**c**) 3 segments; (**d**) 2 segments; and (**e**) 1 segment.

Method 1: The 9 segments in Figure 11 are assigned the GOES magnetization characteristics measured at 10°, 20°, 30°, 40°, 50°, 60°, 70°, 80°, and 90° shown in Figure 3.

Method 2: The 5 segments in Figure 11b are assigned the GOES magnetization characteristics measured at 10°, 30°, 60°, 80°, and 90° shown in Figure 3.

Method 3: The 3 segments in Figure 11c are assigned the GOES magnetization characteristics measured at 30°, 60°, and 90° shown in Figure 3.

Methods 4–5: The 2 segments in Figure 11d are assigned the GOES magnetization characteristics measured at 30° and 90° or 60° and 90° shown in Figure 3, respectively.

Method 6: The 1 segment in Figure 11e is assigned the GOES magnetization characteristics measured at 90°, as shown in Figure 3.

Each method calculates the SOST motor performance under no-load, rated load, and overload conditions. The results are summarized and compared in Table 2.

Table 2. Comparison of six SOST model methods.

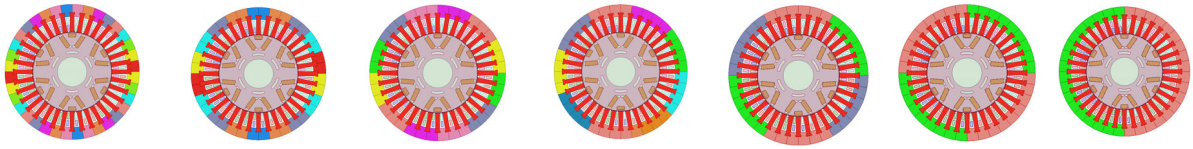
States	Parameters	Method 1	Method 2	Method 3	Method 4	Method 5	Method 6
No-load	E (V)	254	254	254	254	254	250
	B_δ (T)	0.75	0.75	0.75	0.75	0.75	0.75
	T_{cog} (Nm)	0.306	0.304	0.306	0.304	0.314	0.320
Rated load	E (V)	365	365	364	364	363	360
	T (Nm)	60	60	59	60	59	58
	P_{Fe} (W)	486	500	464	437	531	545
Overload	E (V)	354	354	353	354	352	350
	T (Nm)	212	213	212	213	211	209
	P_{Fe} (W)	545	558	533	509	597	611

5. Modeling Method for GOES Stator Yoke

The full-circle stator yoke (FCSY) and fan-shape stator yoke (FSSY) are two typical shapes of GOES stator yokes. For these two yoke shapes, the DSST stator tooth structure is used. The motor performances under no-load, rated load, and overload conditions are analyzed by studying different modeling methods to identify the most suitable modeling method for the stator yoke parts of the FCSY and FSSY. This will provide rapid and accurate modeling methods and principles for GOES yokes, simplifying the modeling steps while maintaining high calculation accuracy.

5.1. FCSY

The GOES FCSY is a full circle with stator teeth embedded in the yoke. Different magnetization characteristic definition methods are designed, and the motor performance is calculated under various conditions when the full circular yoke is divided into 36, 18, 12, 9, 6, 4, and 2 segments, as shown in Figure 12.



(**a**) (**b**) (**c**) (**d**) (**e**) (**f**) (**g**)

Figure 12. Segmentation of the FCSY: (**a**) 36 segments; (**b**) 18 segments; (**c**) 12 segments; (**d**) 9 segments; (**e**) 6 segments; (**f**) 4 segments; and (**g**) 2 segments.

Regions with the same color are assigned the same magnetization characteristics, and seven methods can be designed for the FCSY stator yoke as follows:

Method 1: For the 36 segments in Figure 12a, starting from the red yoke segment, each is assigned the GOES magnetization characteristics measured at 0°, 10°, 20°, 30°, 40°, 50°, 60°, 70°, 80°, 90°, 80°, 70°, 60°, 50°, 40°, 30°, 20°, and 10°, and the pattern repeats around the circle.

Method 2: For the 18 segments in Figure 12b, starting from the red yoke segment, each is assigned the GOES magnetization characteristics measured at 0°, 30°, 50°, 70°, 90°, 70°, 50°, 30°, and 10°, and the pattern repeats around the circle.

Method 3: For the 12 segments in Figure 11c, starting from the yellow yoke segment, each is assigned the GOES magnetization characteristics measured at 10°, 40°, 70°, 80°, 50°, and 20°, and the pattern repeats around the circle.

Method 4: For the 9 segments in Figure 12d, starting from the green yoke segment, each is assigned the GOES magnetization characteristics measured at 20°, 60°, 80°, 50°, 10°, 40°, 80°, 70°, and 30°, and the pattern repeats around the circle.

Method 5: 6 segments: As shown in Figure 12e, starting from the green yoke, each yoke segment is assigned the magnetization characteristics of GOES at 30°, 90°, 40°, 30°, 90°, and 40°, and the pattern repeats around the circle.

Method 6: For the 4 segments in Figure 12f, starting from the green yoke segment, each is assigned the GOES magnetization characteristics measured at 40° and 50°, and the pattern repeats around the circle.

Method 7: For the 2 segments in Figure 12g, starting from the red yoke segment, each is assigned the GOES magnetization characteristics of GOES at 90°.

Table 3 compares the performance of the seven modeling methods under no-load, rated load, and overload conditions. When assigning magnetization characteristics to FCSY, the simulation result converges when the number of segments exceeds 12, and the accuracy increases as the number of segments increases. For computational convenience, the FCSY yoke should be divided into segments such that the angle of each segment does not exceed 30° to ensure accurate results.

Table 3. Comparison of seven FCSY model methods.

States	Parameters	Method 1	Method 2	Method 3	Method 4	Method 5	Method 6	Method 7
No-load	E (V)	253	252	246	246	246	246	246
	B_δ (T)	0.75	0.75	0.75	0.75	0.75	0.75	0.75
	T_{cog} (Nm)	1.27	1.27	1.27	1.21	1.21	1.21	1.22
Rated load	E (V)	360	359	350	350	350	349	350
	T (Nm)	58	58	57	56	56	56	56
	P_{Fe} (W)	523	523	545	563	568	569	563
Overload	E (V)	353	352	339	342	342	339	341
	T (Nm)	212	209	204	201	202	199	201
	P_{Fe} (W)	0.605	0.608	0.623	0.625	0.624	0.631	0.628

5.2. FSSY

The FSSY stator yoke model is composed of multiple parts with the same arc, and the stator teeth are embedded in the yoke as follows:

When the stator yoke of the model is composed of 4 parts, the central angle of each part is 90°. First, assign the GOES magnetization characteristics at 60° to each part, as shown in Figure 13a, and calculate the motor performance. Next, subdivide each part into 3 segments, assigning the GOES magnetization characteristics at 10°, 40°, and 70°, respectively, as shown in Figure 13b, and calculate the motor performance. Finally, subdivide each part into 9 segments; assign the GOES magnetization characteristics at 0°, 10°, 20°, 30°, 40°, 50°, 60°, 70°, and 80°, respectively, as shown in Figure 13c, and calculate the motor performance.

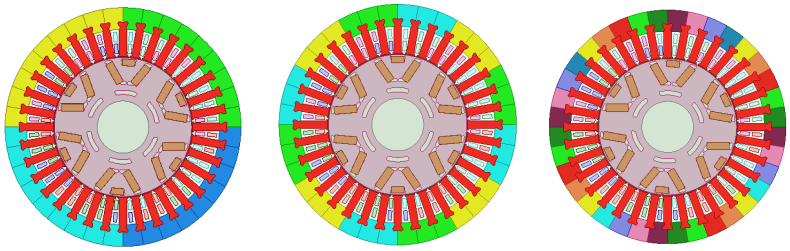


Figure 13. FSSY stator yoke modeling methods for 4 parts: (**a**) 4 parts; (**b**) 4 parts—3 subdivisions; (**c**) 4 parts—9 subdivisions.

When the stator yoke of the model is composed of 6 parts, the central angle of each part is 60°. First, assign the GOES magnetization characteristics at 30° to each part, as shown in Figure 14a, and calculate the motor performance. Next, subdivide each part into 3 segments; assign the GOES magnetization characteristics at 0°, 30°, and 50°, respectively, as shown in Figure 14b, and calculate the motor performance. Finally, subdivide each part into 6 segments; assign the GOES magnetization characteristics at 0°, 10°, 20°, 30°, 40°, and 50°, respectively, as shown in Figure 14c, and calculate the motor performance.

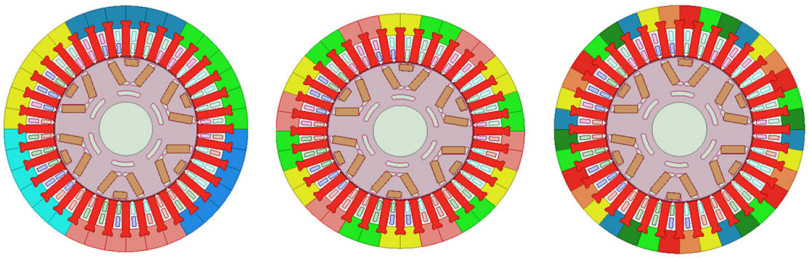
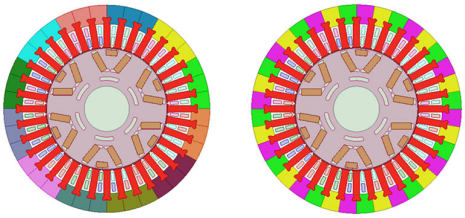


Figure 14. FSSY stator yoke modeling methods for 6 parts: (**a**) 6 parts; (**b**) 6 parts—3 subdivisions; (**c**) 6 parts—6 subdivisions.

When the stator yoke of the model is composed of 12 parts, the central angle of each part is 30°. First, assign the GOES magnetization characteristics at 30° to each part, as shown in Figure 15a, and calculate the motor performance. Next, subdivide each part into 3 segments; assign the GOES magnetization characteristics at 0°, 10°, and 20°, respectively, as shown in Figure 15b, and calculate the motor performance.



(**a**) (**b**)

Figure 15. FSSY stator yoke modeling methods for 12 parts: (**a**) 12 parts; (**b**) 12 parts—3 subdivisions.

Three FSSY topologies were designed, resulting in eight magnetization characteristic definition methods, corresponding to those shown in Figure 13a–c, Figure 14a–c, and Figure 15a,b, respectively. The performance under no-load, rated load, and overload conditions for these eight modeling methods were compared in Table 4.

Table 4. Comparison of eight FSSY model methods.

States	Parameters	Method 1	Method 2	Method 3	Method 4	Method 5	Method 6	Method 7	Method 8
No-load	E (V)	253	253	247	253	253	253	253	253
	B_δ (T)	0.75	0.75	0.75	0.75	0.75	0.75	0.75	0.75
	T_{cog} (Nm)	1.27	1.27	1.28	1.26	1.31	1.31	1.25	1.26
Rated load	E (V)	360	360	360	360	360	360	361	361
	T (Nm)	57	57	57	57	57	57	57	57
	P_{Fe} (W)	540	465	468	466	466	488	444	465
Overload	E (V)	353	353	353	356	354	354	361	360
	T (Nm)	207	207	208	210	207	207	212	211
	P_{Fe} (W)	653	507	628	534	544	558	512	526

Simulation analysis reveals the following:

(1) For a single 90° part of FSSY, assigning the same magnetization characteristics to the entire part significantly deviates from actual magnetic circuit angles, leading to considerable calculation errors. Subdividing the part into smaller segments that align more closely with the actual magnetic circuit directions yields more accurate results. For ease of calculation, when subdividing the part, ensure that the angle of each sub-part does not exceed 30°, which minimizes calculation errors.

(2) For a single 60° part of FSSY, the calculation results show minimal deviation between the whole part calculation and the subdivided part calculation. When subdivided, there is an imbalance in the three-phase voltage under overload conditions, resulting in relatively higher losses. Assigning the same magnetization characteristics to the entire part is advisable for convenient calculation.

(3) For a single 30° part of FSSY, there is minimal deviation between the whole part calculation and the subdivided part calculation. When subdivided, losses are relatively higher. Assigning the same magnetization characteristics to the entire part is advisable for convenient calculation.

Therefore, when a stator yoke comprises more than six parts, each can be assigned the same magnetization characteristics. When the stator yoke is composed of fewer than six parts, it is best to subdivide each part and define different magnetization characteristics to ensure higher calculation accuracy.

6. Topology Optimization of the GOES Stator Core

A separate or integrated stator teeth–yoke structure can be adopted when using GOES to manufacture the stator core.

6.1. Impact of Teeth Shape on Motor Performance

In this section, the stator yoke is assembled from 36 parts of GOES, and the teeth use DSST and SOST structures. We compare and analyze the electromagnetic performance of the motor under no-load, rated load, and overload conditions with different stator teeth structures to determine the optimal stator teeth–yoke assembly method. For DSST, the stator teeth–yoke joint area is assigned GOES magnetization characteristics at 60°. For SOST, the stator teeth–yoke joint is divided into two segments, with each segment along the radial direction from inside to outside being assigned the GOES magnetization characteristics at 60° and 90°, respectively.

Table 5 compares both design schemes' performance under no-load, rated load, and overload conditions. The simulation results show that in the DSST structure, the teeth embedded in the yoke are positioned lower than the point where the magnetic field linearly changes direction, resulting in better magnetic conductivity. In contrast, the SOST structure has parts where the direction of magnetic conductivity is perpendicular to the rolling direction, leading to poorer magnetic conductivity. Therefore, the performance of the DSST structure is superior.

Table 5. Comparison of DSST and SOST.

States	Parameters	DSST	SOST
No-load	E (V)	254	254
	B_δ (T)	0.75	0.75
	T_{cog} (Nm)	0.475	0.291
Rated load	E (V)	377	364
	T (Nm)	60	59
	P_{Fe} (W)	489	510
Overload	E (V)	365	357
	T (Nm)	219	214
	P_{Fe} (W)	497	0.529

6.2. Impact of Yoke Shape on Motor Performance

Based on the previous analysis, the optimal teeth structure selected is the DSST structure. Then, we analyze the motor performance under different loads with varying topologies of the stator yoke. In this section, the stator yoke adopts a FSSY structure, with the number of parts being 36, 18, 9, 3, 2, and 1. Taking the motor with 18 parts as an example, Figure 16 illustrates the GOES rolling directions for both the teeth and yoke during the stator core stamping process.

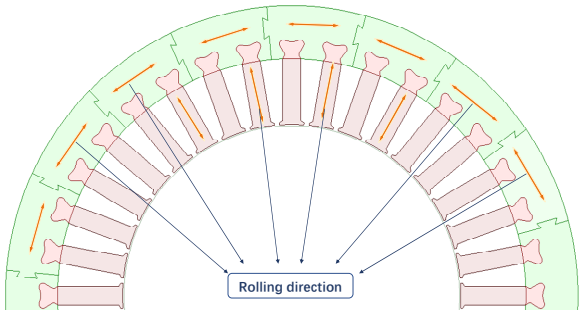


Figure 16. Rolling directions of GOES stator.

Seven different FSSY stators have been designed by assigning the magnetic properties of each part as follows:

Motor 1: For the 36 parts in Figure 17a, each is assigned the GOES magnetic properties at 0°.

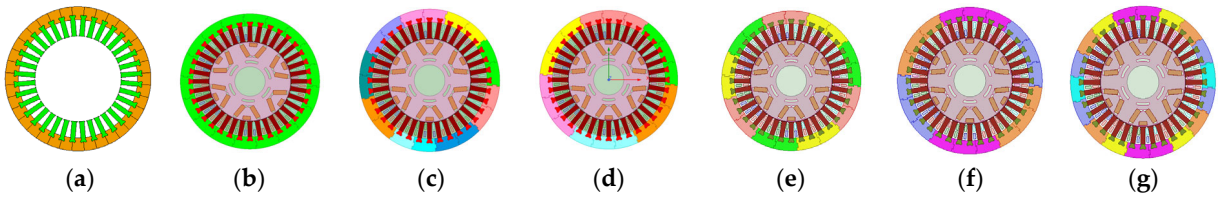


Figure 17. Seven schemes of FSSY motor: (**a**) 36 parts; (**b**) 18 parts; (**c**) 9 parts; (**d**) 6 parts; (**e**) 3 parts; (**f**) 2 parts; (**g**) 1 part.

Motor 2: For the 18 parts in Figure 17b, each is assigned the GOES magnetic properties at 0°.

Motor 3: For the 9 parts in Figure 17c, each is assigned the GOES magnetic properties at 10°.

Motor 4: For the 6 parts in Figure 17d, each is assigned the GOES magnetic properties at 20°.

Motor 5: For the 3 parts in Figure 17e, each is assigned the GOES magnetic properties at 10°, 50°, and 90°, respectively.

Motor 6: For the 2 parts in Figure 17f, each is assigned the GOES magnetic properties at 20°, 80°, and 40°, respectively.

Motor 7: For the 1 part (FCSY) in Figure 17g, it is assigned GOES magnetic properties at 0°, 20°, 40°, 60°, 80°, 60°, 40°, and 20°, repeated throughout the yoke.

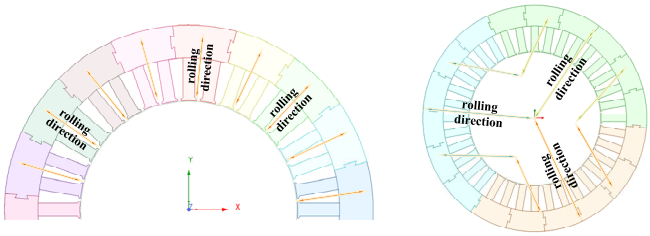
The performance of these seven motors was calculated under no-load, rated load, and overload conditions. The results are summarized and compared in Table 6. As the number of parts in the stator yoke decreases, the motor torque under the light load and overload gradually decreases while the core losses increase. The more fan-shaped parts in the stator, the better the motor's electromagnetic performance.

Table 6. Comparison of seven FSSY motors.

States	Parameters	Motor 1	Motor 2	Motor 3	Motor 4	Motor 5	Motor 6	Motor 7
No-load	E (V)	254	252	252	252	252	251	252
	B_δ (T)	0.75	0.75	0.75	0.75	0.75	0.75	0.75
	T_{cog} (Nm)	0.475	1.31	1.32	1.33	1.39	1.34	1.34
Rated load	E (V)	377	374	372	372	368	364	360
	T (Nm)	60	59	58	58	56	55	53
	P_{Fe} (W)	489	477	498	537	537	545	544
Overload	E (V)	365	364	362	358	350	346	345
	T (Nm)	219	214	214	212	209	206	205
	P_{Fe} (W)	497	504	531	586	595	593	629

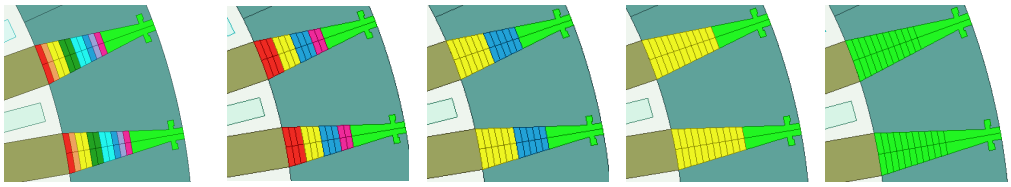
6.3. Impact of TYIS on Motor Performance

Six types of TYIS stator structures are designed, including 18 parts (2 teeth and 1 yoke), 9 parts (4 teeth and 1 yoke), 6 parts (6 teeth and 1 yoke), 3 parts (12 teeth and 1 yoke), and a single part (36 teeth and 1 yoke). Figure 18 illustrates GOES's rolling direction in the TYIS stator teeth of the 18-part (2 teeth and 1 yoke) and 3-part (12 teeth and 1 yoke) configurations. The magnetic properties in each part are assigned as Figure 19:



(**a**) (**b**)

Figure 18. Rolling directions of TYIS: (**a**) 18 parts; (**b**) 3 parts.



(**a**) (**b**) (**c**) (**d**) (**e**)

Figure 19. Five TYIS motors: (**a**) 18 parts; (**b**) 9 parts; (**c**) 6 parts; (**d**) 3 parts; (**e**) 1 part.

Motor 1: For the 18 parts in Figure 19a, the stator teeth are assigned the GOES magnetization characteristics at 0° and the yoke at 90°.

Motor 2: For the nine parts in Figure 19b, the four teeth associated with each sector are assigned as follows: the two middle teeth are given the GOES magnetization characteristics at 0°, while the two outer teeth are assigned the GOES magnetization characteristics at 10°. The yoke is assigned the GOES magnetization characteristics at 80°.

Motor 3: For the six parts in Figure 19c, the six teeth associated with a single sector are assigned as follows: the two middle teeth are given the GOES magnetization characteristics at 0°, while the remaining four teeth are assigned the GOES magnetization characteristics at 10° and 20° from inner to outer. The yoke is divided into three segments, with the middle segment assigned the GOES magnetization characteristics at 90° and the two outer segments assigned the GOES characteristics at 80°.

Motor 4: For the three parts in Figure 19d, the twelve teeth associated with a single sector are assigned as follows: the two middle teeth are given the GOES magnetization characteristics at 0°, while the remaining eight teeth are assigned the GOES magnetization characteristics at 10°, 20°, 30°, 40°, and 50° from inner to outer. The yoke is divided into six segments, with the middle segment assigned the GOES magnetization characteristics at 80° and the two outer segments the GOES magnetization characteristics at 60° and 40° from the middle outward.

Motor 5: For the full circle in Figure 19e, the model is divided into two segments, with 18 teeth associated with the semi-circle unit. The two middle teeth are assigned the GOES magnetization characteristics at 0°. In comparison, the remaining 16 teeth are assigned the GOES magnetization characteristics at 10°, 20°, 30°, 40°, 50°, 60°, 70°, and 80° from inner to outer. The semi-circle model of the yoke is divided into nine segments, with the middle segment assigned the GOES magnetization characteristics at 90° and the two outer segments assigned the GOES magnetization characteristics at 70°, 50°, 30°, and 10° from the middle outward.

Table 7 compares the performances of the five designs under no-load, rated load, and overload conditions. The simulation results show that the motor's performance gradually deteriorates as the sector's angle increases. Additionally, when the arc angle of a single sector exceeds 60°, the motor exhibits varying degrees of three-phase voltage imbalance under load conditions. When the angle of a single sector exceeds 120°, the magnetic flux density decreases, and the losses are reduced.

Table 7. Comparison of five TYIS motors.

States	Parameters	Motor 1	Motor 2	Motor 3	Motor 4	Motor 5
No-load	E (V)	251	251	249	249	246
	B_δ (T)	0.75	0.75	0.75	0.75	0.75
	T_{cog} (Nm)	0.734	0.734	0.757	0.828	0.855
Rated load	E (V)	371	371	370	360	357
	T (Nm)	60	59	58	56	55
	P_{Fe} (W)	536	592	634	564	541
Overload	E (V)	352	350	350	347	345
	T (Nm)	212	211	210	205	202
	P_{Fe} (W)	563	624	677	606	602

6.4. Performance Comparison of Different GOES Motors

Based on the comprehensive analysis above, the motor with DSST and 36-part yoke structure exhibits the best performance and is designated Motor 1. In addition, two additional reference motors, designated Motors 2 and 3, are introduced to compare the performance differences between GOES and NOES motors. Motor 2 is a motor with the stator yoke made of NOES and the stator teeth made of GOES. Motor 3 is a standard NOES motor, with the stator of NOES material processed into a single part.

Table 8 compares the performances of Motors 1, 2, and 3. Motor 1, with its DSST stator and 36-part yoke, has the lowest no-load back EMF and lowest output torque, core losses, and total harmonic distortion (THD) in the back EMF under load conditions. Motor 2 exhibits the highest no-load back EMF and highest output torque under load conditions, but its core losses and THD in the back EMF are also high. Motor 3 has a no-load back EMF close to that of Motor 2. However, its output torque is lower, and the core losses are the highest under load states.

Table 8. Comparison of different motor designs.

States	Parameters	Motor 1	Motor 2	Motor 3
No-load	E (V)	254	284	283
	B_δ (T)	0.75	0.84	0.84
	T_{cog} (Nm)	0.475	0.720	0.350
Rated load	E (V)	377	372	362
	THD of E	2.14‰	1.52‰	1.22‰
	T (Nm)	60	63	61
	P_{Fe} (W)	489	524	515
Overload	E (V)	365	350	336
	THD of E	1.04‰	2.28‰	1.70‰
	T (Nm)	219	225	218
	P_{Fe} (W)	497	544	560

7. Experimental Performance Testing of the GOES Motors

Three prototypes, designated as Motors 1, 2, and 3, the same as those in Section 6.4, were fabricated and tested to verify the accuracy of simulation results and theoretical analysis. Motor 1 features a stator with a DSST structure, with the teeth and yoke made of GOES 27SGQ1400. Motor 2 has a stator yoke made of NOES 27SW1400 in a full-circle configuration, while the teeth are made of GOES 27SGQ1400. Motor 3 uses NOES 27SW1400 for both the stator teeth and yoke, representing a standard NOES motor. The loss density of 27SW1400 is significantly higher than that of 27SQG120.

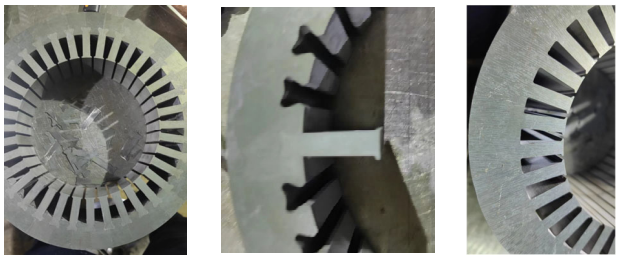
7.1. Experimental Setup

The experiments were conducted in a specialized electric vehicle motor testing laboratory. The lab layout includes a control room, a test room, and an equipment room, with the dynamometer frequency converter and battery simulator placed in the equipment room to minimize interference with the test data, as shown in Figure 20. The laboratory is equipped with equipment and systems imported from AVL List GmbH of Austria, boasting a maximum speed of 20,000 rpm, a maximum power of 312 kW and a maximum torque of 625 Nm. Its configurations include a battery simulator, a damp-heat environmental chamber dual-channel temperature control units for motors and controllers, and a chilled water unit, as well as three-directional vibration sensors for vibration monitoring of the tested motors. Figure 21 shows the photos of the stator cores of the three prototypes.



(**a**) (**b**) (**c**)

Figure 20. Motor testing laboratory: (**a**) control room; (**b**) test room; (**c**) equipment room.



(**a**) (**b**) (**c**)

Figure 21. Stator cores of the three prototypes: (**a**) Motor 1; (**b**) Motor 2; (**c**) Motor 3.

7.2. Experimental Testing

For the three prototypes, both electromagnetic and thermal rise tests were performed. Parameters such as maximum torque, highest efficiency, average efficiency, CLTC (China Light-Duty Vehicle Test Cycle) efficiency, high-efficiency zone percentage, steady-state temperature rise, and peak temperature rise were measured. These results were compared with those from the simulation models to comprehensively analyze the performance of the motors under different stator core configurations: GOES-only, GOES teeth with NOES yoke, and NOES-only.

The three prototypes were tested over a speed range of 500–18,000 rpm with a bus voltage of 540 V. The test results are summarized in Table 9.

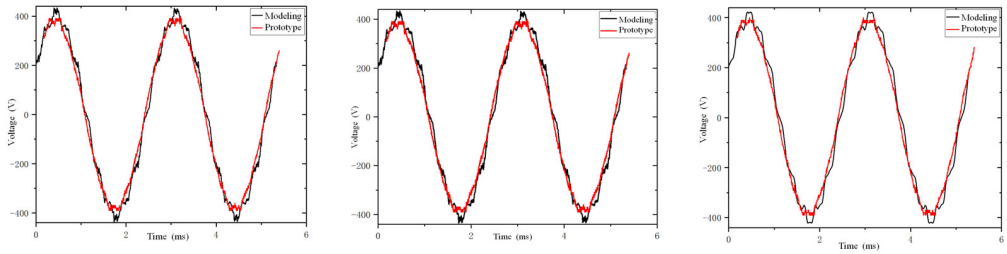
Table 9. Test data for three prototypes.

Parameters	Motor 1	Motor 2	Motor 3
Back *EMF* (V)	260.5	271.4	273.9
Max Torque (Nm)	215.6	219	215.3
Max Power (kW)	123.75	124.16	124.58

Table 9. *Cont.*

Parameters	Motor 1	Motor 2	Motor 3
Max Efficiency (%)	97.41	97.16	97.6
Average Efficiency (%)	92.77	92.9	93.17
CLTC Efficiency (%)	94.32%	94.60%	94.75%
85% Efficiency Zone Proportion (%)	90.99	91.28	91.91
90% Efficiency Zone Proportion (%)	83.02	83.02	84.01
95% Efficiency Zone Proportion (%)	54.46	55.57	58.61

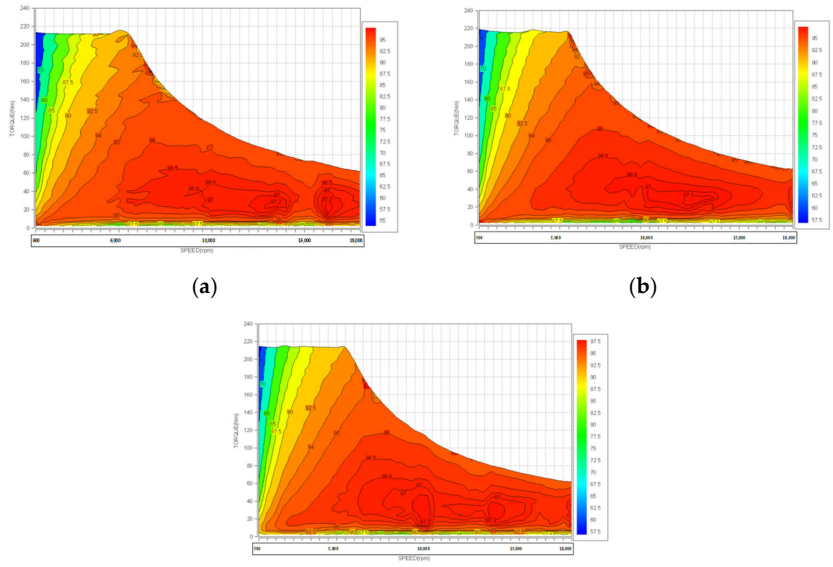
Table 9 shows that the efficiency and power performance from Motor 1 to Motor 3 progressively improve, but the output torque of Motor 2 is the highest, consistent with the simulation analysis results. Comparing the no-load back EMF curves of the simulation models and the prototype tests, as shown in Figure 22, it is evident that the simulation and experimental data closely match. All three motors' no-load back EMF errors are within 5%, considered within a reasonable range.



(**a**) (**b**) (**c**)

Figure 22. Comparison of measured and simulated no-load back EMF curves: (**a**) Motor 1; (**b**) Motor 2; (**c**) Motor 3.

Figure 23 shows the efficiency maps of the three prototypes. Combined with the data in the table, it can be seen that Motor 3 has the largest area coverage at the same efficiency level, and its high-efficiency area is also closer to the commonly used speed range during driving.



(**a**) (**b**)

(**c**)

Figure 23. Efficiency maps: (**a**) Motor 1; (**b**) Motor 2; (**c**) Motor 3.

Figure 24 compares the torque–speed (T-n) and output power–speed (P-n) cures of the three prototypes, and the trend of the characteristic curves for all three prototypes is consistent.

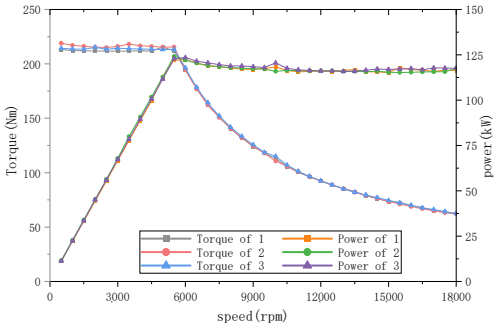


Figure 24. T-n and P-n curves of the three prototypes.

Figure 25 shows the temperature rise of the three prototypes during operation, with a test water temperature of 60 °C. As shown, Motor 1 has the slowest temperature rise under peak conditions. In contrast, Motor 3 has the fastest temperature rise and the shortest duration of peak operation, requiring better cooling and insulation protection. Under the rated conditions, Motors 1 and 3 have the highest steady-state temperature rise. In contrast, Motor 2 has the lowest steady-state temperature rise, which is more conducive to long-term stable operation.

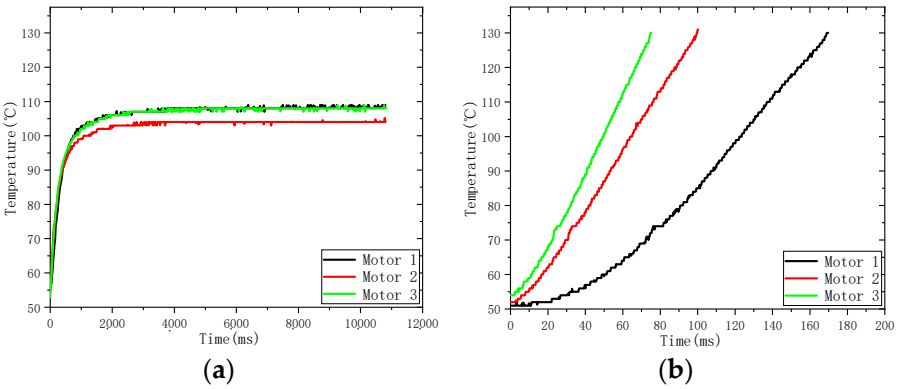


Figure 25. Temperature curves of the three prototypes: (**a**) rated temperature; (**b**) peak temperature.

A comprehensive analysis of the three prototypes' electromagnetic and temperature rise parameters reveals that Motor 1 has the slowest transient temperature rise, making it beneficial for prolonged overload operation. Motor 2 has the lowest steady-state temperature rise, enhancing the motor's lifespan and operational safety, and has the highest output torque. Motor 3 has high efficiency and output power, making it suitable for applications with high-efficiency requirements.

When the motors operate at rated conditions (rotational speed of 7500 rpm, frequency of 375 Hz, and current of 90 A), the magnetic flux density of the motor cores is low. Under such operating conditions, the difference in core losses between the two silicon steel sheets 27SQG120 and 27SW1400 that constitute the cores is not significant. Considering multiple factors such as the loss difference between the two silicon steel sheets, the splicing gaps of the stator teeth and yokes, and the performance degradation caused by punching and shearing processes, the rated temperature rises of Motor 1 and Motor 3 are basically equivalent, while that of Motor 2 is relatively lower. When the motors operate at peak conditions (rotational speed of 7500 rpm, frequency of 375 Hz, and current of 300 A), the

magnetic flux density of the motor cores is high. Under such operating conditions, the difference in core losses between the two silicon steel sheets 27SQG120 and 27SW1400 that constitute the cores is quite significant, with 27SQG120 exhibiting a remarkable loss advantage. Therefore, the core losses of Motor 1, which is entirely fabricated with 27SQG120, and Motor 2, whose stator teeth are made of 27SQG120, are relatively low, and their peak temperature rises are accordingly lower as well.

8. Conclusions

Using the PMSM as an example, this paper investigates the topological structures and modeling methods of using GOES to improve motor power density. Three prototypes of different stator structures are fabricated and experimentally tested. The following conclusions can be drawn from this study:

The comparative study of various GOES PMSM stator core modeling methods can be summarized as follows. For the stator teeth, the modeling methods of the DSST and SOST stator cores were analyzed. When using the DSST model, the depth of the dovetail slot joining the teeth and yoke should not exceed the bending position of the magnetic circuit direction. This allows the stator teeth –yoke joint to be assigned as a whole, simplifying the calculation. When using the SOST model, the finer the subdivision according to the magnetic circuit direction, the more accurate the results. Both the FCSY and FSSY were analyzed for the stator yoke. When using the FCSY model, the calculation results are more accurate if the part angle is less than 30°. When using the FSSY model, a single 30° part can be assigned as a whole for calculation.

An optimal stator core structure is found using the newly researched GOES PMSM stator core modeling methods. The analysis reveals that the motor performance of the DSST stator is superior to that of the SOST stator. Subsequently, taking the DSST motor as the research object, the results show that when the angle of a single FSSY unit is less than 60°, the deviation in the motor's electrical performance parameters is minimal. The performance simulation results of the TYIS motor reveal that as the angle of the SSSY unit increases, the electromagnetic performance gradually deteriorates. The numerical comparison of GOES PMSMs of different stator structures and the benchmark NOES motor shows that the electromagnetic performance of Motor 2, a hybrid motor with NOES yoke and GOES teeth, is superior.

Three prototypes were fabricated and tested. The discrepancy between the experimental and simulation results is less than 5%, validating the accuracy of the simulation analysis.

Author Contributions: Conceptualization, G.L. and J.Z. (Jing Zhao); methodology, G.L.; software, G.L. and X.G.; validation, G.L., J.Z. (Jing Zhao) and X.G.; formal analysis, J.Z. (Jing Zhao); investigation, G.L. and Z.H.; resources, Z.H.; data curation, J.Z. (Jianguo Zhu) and X.G.; writing—original draft preparation, G.L.; writing—review and editing, J.Z. (Jianguo Zhu); visualization, X.G.; supervision, J.Z. (Jing Zhao); project administration, J.Z. (Jing Zhao); funding acquisition, J.Z. All authors have read and agreed to the published version of the manuscript.

Funding: This research received no external funding.

Data Availability Statement: The datasets presented in this article are not readily available due to technical and time limitations. Requests to access the datasets should be directed to zhaojing_bit@bit.edu.cn.

Conflicts of Interest: Authors Guanglin Li and Zhiyuan Hu were employed by the company Shougang Zhixin Electromagnetic Material (Qian'an) Co., Ltd. All the authors declare that the research was conducted in the absence of any commercial or financial relationships that could be construed as a potential conflict of interest.

References

1. Shao, L.; Navaratne, R.; Popescu, M.; Liu, G. Design and Construction of Axial-Flux Permanent Magnet Motors for Electric Propulsion Applications—A Review. *IEEE Access* **2021**, *9*, 158998–159017. [CrossRef]
2. Murataliyev, M.; Degano, M.; Di Nardo, M.; Bianchi, N.; Gerada, C. Synchronous Reluctance Machines: A Comprehensive Review and Technology Comparison. *Proc. IEEE* **2022**, *110*, 382–399. [CrossRef]
3. Nugraha, Y.U.; Asfani, D.A.; Negara, I.M.Y.; Aziz, M.; Yuniarto, M.N. Technology Review of Electric Motor for Hybrid-Electric Vehicle. In Proceedings of the 2021 IEEE Region 10 Conference (TENCON), Auckland, New Zealand, 7–10 December 2021; pp. 777–781.
4. Liu, C.; Chau, K.T.; Lee, C.H.T.; Song, Z. A Critical Review of Advanced Electric Machines and Control Strategies for Electric Vehicles. *Proc. IEEE* **2021**, *109*, 1004–1028. [CrossRef]
5. Bird, J.Z. A Review of Electric Aircraft Drivetrain Motor Technology. *IEEE Trans. Magn.* **2022**, *58*, 8201108. [CrossRef]
6. Aloeyi, E.F.; Ali, N.; Wang, Q. A Review of In-Wheel Motors for Electric Vehicle Propulsion. In Proceedings of the 2022 IEEE Transportation Electrification Conference and Expo, Asia-Pacific (ITEC Asia-Pacific), Haining, China, 28–31 October 2022; pp. 1–6.
7. Ou, J.; Liu, Y.; Doppelbauer, M. Comparison Study of a Surface-Mounted PM Rotor and an Interior PM Rotor Made from Amorphous Metal of High-Speed Motors. *IEEE Trans. Ind. Electron.* **2021**, *68*, 9148–9159. [CrossRef]
8. Ibrahim, M.; Bernier, F.; Lamarre, J.M. Novel Multi-layer Design and Additive Manufacturing Fabrication of a High Power Density and Efficiency Interior PM Motor. In Proceedings of the 2020 IEEE Energy Conversion Congress and Exposition (ECCE), Detroit, MI, USA, 11–15 October 2020; pp. 3601–3606.
9. Wang, X.; Zhou, S.; Wu, L.; Zhao, M.; Hu, C. Iron Loss and Thermal Analysis of High Speed PM Motor Using Soft Magnetic Composite Material. In Proceedings of the The 22nd International Conference on Electrical Machines and Systems (ICEMS), Harbin, China, 11–14 August 2019; pp. 1–4.
10. Ou, J.; Liu, Y.; Schiefer, M.; Breining, P.; Doppelbauer, M.; Chai, F. Application of Amorphous Cores to DC-excited Flux-modulated Motors Used for Electric Vehicles. In Proceedings of the 2018 IEEE International Conference on Electrical Systems for Aircraft, Railway, Ship Propulsion and Road Vehicles & International Transportation Electrification Conference (ESARS-ITEC), Nottingham, UK, 7–9 November 2018; pp. 1–7.
11. Kim, K.O.; Jung, Y.H.; Park, J.C.; Lim, M.S. Comparative study of Mechanical and Electrical Characteristics on High-Strength Steel and Conventional Steel for EV Traction High-Speed Multilayer IPMSM Using Rare-Earth Free PM. In Proceedings of the 2023 IEEE International Magnetic Conference (INTERMAG), Sendai, Japan, 15–19 May 2023; pp. 1–2.
12. Wang, S.; Ma, J.; Liu, C.; Wang, Y.; Lei, G.; Guo, Y.; Zhu, J. Design and performance analysis of a novel PM assisted synchronous reluctance machine. *Int. J. Appl. Electromagn. Mech.* **2021**, *67*, 131–140. [CrossRef]
13. Zhang, S.; Liu, C.; Wang, S.; Wang, Y.; Zhu, J. Preliminary Design and Comparative Analysis of a New Synchronous Reluctance Machine with Hybrid Cores. *IEEE Trans. Magn.* **2023**, *59*, 8103205. [CrossRef]
14. Liu, C.; Wang, K.; Wang, S.; Wang, Y.; Zhu, J. Torque ripple reduction of synchronous reluctance machine by using asymmetrical barriers and hybrid magnetic core. *CES Trans. Electr. Mach. Syst.* **2021**, *5*, 13–20. [CrossRef]
15. Wu, Q.; Guo, X.; Lin, Q.; Pang, J.; Lu, C. Design and Optimization of Permanent-Magnet Vernier Machine with Split-teeth Stator based on Grain-Oriented Silicon Steel. In Proceedings of the the 26th International Conference on Electrical Machines and Systems (ICEMS), Zhuhai, China, 5–8 November 2023; pp. 5089–5093.
16. Talebi, D.; Gardner, M.C.; Sankarraman, S.V.; Daniar, A.; Toliyat, H.A. Electromagnetic Design Characterization of a Dual Rotor Axial Flux Motor for Electric Aircraft. *IEEE Trans. Ind. Appl.* **2022**, *58*, 7088–7098. [CrossRef]
17. Ozdincer, B.; Aydin, M. Design of Innovative Radial Flux Permanent Magnet Motor Alternatives with Non-Oriented and Grain-Oriented Electrical Steel for Servo Applications. *IEEE Trans. Magn.* **2022**, *58*, 8200304. [CrossRef]
18. Rebhaoui, A.; Randi, S.A.; Demian, C.; Lecointe, J.-P. Analysis of Flux Density and Iron Loss Distributions in Segmented Magnetic Circuits Made with Mixed Electrical Steel Grades. *IEEE Trans. Magn.* **2022**, *58*, 2000711. [CrossRef]
19. Li, Z.; Ma, Y.; Hu, A.; Zeng, L.; Xu, S.; Pei, R. Investigation and Application of Magnetic Properties of Ultra-Thin Grain-Oriented Silicon Steel Sheets under Multi-Physical Field Coupling. *Materials* **2022**, *15*, 8522. [CrossRef] [PubMed]
20. Livadaru, L.; Virlan, B.; Munteanu, A.; Nacu, I.; Simion, A.; Nastas, I. Magnetic Circuit Segmentation Effects on Fractional Slot Concentrated Winding Synchronous Machine with Grain Oriented Electric Steel. In Proceedings of the International Conference on Electromechanical and Energy Systems (SIELMEN), Craiova, Romania, 11–13 October 2023; pp. 1–4.

Disclaimer/Publisher's Note: The statements, opinions and data contained in all publications are solely those of the individual author(s) and contributor(s) and not of MDPI and/or the editor(s). MDPI and/or the editor(s) disclaim responsibility for any injury to people or property resulting from any ideas, methods, instructions or products referred to in the content.